

Diffusion-Weighted and Diffusion Tensor Imaging: Applications in Skeletal Muscles

Usha Sinha and Shantanu Sinha

Contents

1	Key Points	70
2	Introduction	70
3	Diffusion-Weighted Magnetic Resonance Imaging	71
3.1	Isotropic and Restricted Diffusion.....	71
3.2	Anisotropic and Restricted Diffusion.....	71
4	Imaging Pulse Sequences for Diffusion-Weighted Magnetic Resonance Imaging	71
4.1	Spin Echo, Echo Planar Diffusion-Weighted Imaging.....	72
4.2	Stimulated-Echo Planar Diffusion-Weighted Imaging.....	73
5	Post-processing of Diffusion-Weighted Images	74
5.1	Denoising.....	74
5.2	Geometric Distortions from Eddy Currents and Motion.....	74
5.3	Geometric Distortions from Susceptibility Artifacts.....	75
6	Muscle Model of Diffusion	75
7	Diffusion Tensor Indices in the Normal MSK System ...	76
7.1	Diffusion Tensor Imaging Under Passive and Active Muscle Contraction.....	77
8	Fiber Tractography	78
8.1	Fiber Pennation Angles and Fiber Lengths.....	81
9	Diffusion-Weighted and Diffusion Tensor Imaging in Muscle Injury	83
10	Conclusion	83
	References	83

Abstract

Diffusion tensor magnetic resonance imaging (MRI) has been applied until fairly recently to the study of the brain microarchitecture. Muscle diffusion tensor imaging is still in its infancy but opens a whole new area of research in mapping microstructural organization. Diffusion arises from random motions from thermal energy; these random motions are referred to as “Brownian motion.” MRI is the only modality that allows the noninvasive determination of diffusion (which is on the order of microns) and provides an excellent probe into tissue microarchitecture. Diffusion in biological tissue can be both hindered and have a preferential direction. In the latter case, diffusion is said to be anisotropic. In this chapter, we start with a brief discussion of the technical details of diffusion tensor image acquisition and the post-processing methods. The challenges of this complex modality can be appreciated from these technical details. Diffusion is measured at the macroscopic level but reflects micro-level structural organization. Diffusion models enable one to link the microarchitecture to the observed diffusion tensor; a brief discussion of the diffusion models is presented here. The potential to infer physiological status at a microscopic level from macroscopic measurements offers exciting possibilities for understanding muscle physiology and changes with disease. In order to apply this technique to detecting changes with normal progression or disease, it is important to establish normative values as well as the reproducibility of the technique. The summary of normal ranges and reproducibility of the diffusion indices is presented and confirms that the technique can monitor changes of the order of $\sim 8\%$. Several studies using DTI in disease condition are also presented to provide the range of application of diffusion tensor imaging. In addition to scalar indices of diffusion, DTI also enables muscle fiber tracking. Fiber tracking is the most challenging aspect of DTI and results from several

U. Sinha (✉)
Department of Physics, San Diego State University,
San Diego, CA, USA
e-mail: usinha@sciences.sdsu.edu

S. Sinha
Muscle Imaging and Modeling Laboratory,
Department of Radiology, University of California,
San Diego, CA, USA

groups are presented to demonstrate the feasibility and utility of this method in extracting fiber architectural parameters in a way that was not possible till now.

1 Key Points

1. Diffusion-weighted and diffusion tensor imaging of muscle is a novel technique that allows for probing tissue microarchitecture.
 2. Image post-processing for extraction of robust diffusion indices and fiber tracking is presented in this chapter.
 3. Muscle models of diffusion are also presented in this chapter which link microarchitecture to observed diffusion indices.
 4. Muscle fiber tracking and extraction of fiber architecture (length, pennation angle, curvature) is feasible.
 5. Applications of DWI/DTI to monitor skeletal muscle conditions are now evolving as clinically feasible tools.
-

2 Introduction

Diffusion tensor magnetic resonance imaging (MRI) is a relatively recent advancement which allows the *in vivo* study of microstructural organization (Alexander et al. 2007; Assaf and Pasternak 2008; Mukherjee and McKinstry 2006). Diffusion arises from random motions from thermal energy and is referred to as “Brownian motion” (Basser and Jones 2002; Hagmann et al. 2006). MRI is the only modality that allows the noninvasive determination of diffusion and provides an excellent probe into tissue microarchitecture. The proton is the main nucleus of interest in whole-body MRI and the main diffusion studies referred to in most studies is that of the water molecule. In contrast to a pure liquid, diffusion is hindered by the presence of macromolecules and other barriers in tissue, reducing the effective diffusion length. In addition to hindered diffusion, underlying tissue microstructure that presents regularly oriented barriers to water diffusion will selectively limit molecular excursions arising from Brownian motion in specific directions. This is termed as “anisotropic diffusion imaging.” Diffusion anisotropy has been identified in several tissues: white matter, cardiac, skeletal, and lingual muscle (Budzik et al. 2007; Gilbert and Napadow 2005; Mukherjee and McKinstry 2006; Tseng et al. 2003). By far, the maximum number of studies using diffusion tensor imaging has focused on applications in the brain (Shenton et al. 2012; Assaf and Pasternak 2008; Bennett and Rypma 2013). The relative immobility of the brain coupled with

strong anisotropy of white matter fibers and the implication of white matter structural integrity in normal and disease conditions have resulted in intense research in this area.

Muscle diffusion-weighted and diffusion tensor imaging is, by contrast to brain diffusion imaging, a relatively recent development. However, many advances have been made in a short time. Muscle fiber direction determined from diffusion tensor imaging has been validated by direct anatomical examination and by optical imaging (Damon et al. 2002; Napadow et al. 2001). *In vivo* human DTI studies of the calf muscle have also reported the dependency on gender and age as well as the effect of injury (Galbán et al. 2004, 2005; Zaraiskaya et al. 2006). Recent studies have also identified changes in the eigenvalues and fractional anisotropy (FA) as muscle lengths change under passive and active conditions of plantar and dorsi flexion (Deux et al. 2008; Hatakenaka et al. 2008; Okamoto et al. 2010; Schwenger et al. 2009). Models of muscle architecture have been proposed to explain observed diffusion indices in muscle compartments as well differences in age, gender and changes with flexion (Galbán et al. 2004, 2005; Karampinos et al. 2009). Model-based inferences provide an unprecedented way to link macroscopic tissue level findings (diffusion indices from MRI) to cellular level organization allowing the construction of hierarchical multiscale systems. Further, feasibility of tracking muscle fibers from *in vivo* diffusion tensor images of the calf and forearm has been demonstrated (Sinha et al. 2006; Lansdown et al. 2007; Froeling et al. 2012) and extended to more quantitative assessment of fiber tracks such as muscle fiber length and pennation angle (Heemskerk et al. 2009, 2010).

Imaging techniques, using both ultrasound and MRI have provided a wealth of information related to the morphology and functioning of skeletal muscle (Drace and Pelc 1994; Finni et al. 2003; Hatakenaka et al. 2008; Maganaris et al. 1998; Pappas et al. 2002; Shin et al. 2008). One potential goal for imaging is to develop subject-specific data where muscle morphological and mechanical data may be combined to develop more complete descriptions of muscle performance, intersubject variability and changes arising from onset of disease. One important issue in skeletal muscle is the orientation of muscle fibers within a muscle and the potential curvature of those fibers (Muramatsu et al. 2002). The orientation of the fibers influences the physiological cross-sectional area (PCSA) and the relationship between fiber shortening and aponeurosis shear (Azizi et al. 2008; Chi et al. 2010; Shin et al. 2008). Diffusion tensor imaging is emerging as a promising tool for *in vivo* mapping of fiber lengths and pennation angles from true 3D measurements and thus has the potential to advance the understanding of muscle structure and function and enable creation of accurate subject-specific muscle models.

3 Diffusion-Weighted Magnetic Resonance Imaging

Diffusion-weighted imaging refers to mapping the Brownian motion of molecules and in the case of proton imaging, the Brownian motion of water molecules. Brownian motion refers to the random molecular motion due to thermal energy of the system. This random motion called molecular diffusion was first explained by Einstein (1956). It was shown that the displacements in a liquid (e.g., water) could be modeled as a Gaussian distribution in 3D. The width of the Gaussian distribution depends on the type of molecule in the medium, the temperature, as well as the time of observation of the diffusion. The Gaussian displacement can be characterized by a single variable, the variance. In one dimension, the variance, σ^2 , is given by the $2DT$ where D is referred to as the diffusion coefficient and T is the time over which the diffusion is observed. In water, the diffusion coefficient is $3.0 \times 10^{-9} \text{ m}^2/\text{s}$ at 37°C (Hagmann et al. 2006).

3.1 Isotropic and Restricted Diffusion

Consider the case of diffusion if the water molecule is confined to be within objects that are impermeable. If the object dimensions are small and/or the diffusion time, T is long, the water molecule will be restricted to the object dimension. A measurement of the displacement of the water molecules in such a situation will exhibit a Gaussian distribution with a smaller variance reflecting the “restricted diffusion” arising from the water molecule in an impermeable object. The value of the diffusion coefficient will be smaller than the pure water case; restricted diffusion is exhibited by in vivo tissue such as brain gray matter, cerebrospinal fluid, and fat.

3.2 Anisotropic and Restricted Diffusion

In addition to restricted diffusion, molecules can also be in a local environment that is asymmetric (Basser and Jones 2002; Mori and Barker 1999). A microenvironment where the packing is “fiber-like” with impermeable/semi-permeable walls around the fibers will allow diffusion along the fiber length more readily than perpendicular to the fiber. This gives rise to the case of anisotropic, restricted diffusion; this diffusion type is found in the white matter in the brain as well as in muscle fibers.

3.2.1 Muscle Architecture

Skeletal muscle is a complex system with different components: muscle fibers, connective tissue, and blood and

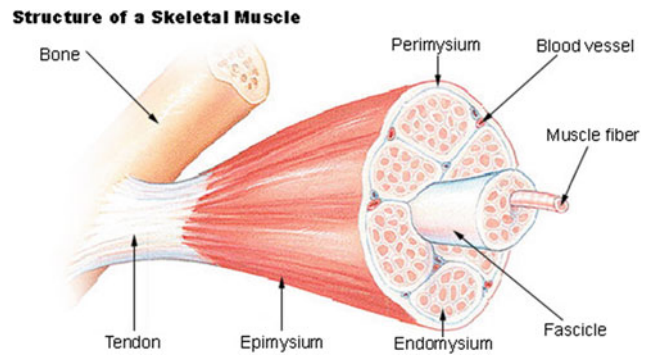


Fig. 1 This figure shows the arrangement of the muscle fibers as well as the connective tissue (endomysium, perimysium, and epimysium) surrounding the muscle fiber, bundles of muscle fiber, and the whole muscle compartment, respectively. Diffusion anisotropy can be understood in the context of the muscle fiber arrangement [Reprinted from SEER training modules, ‘Structure of Skeletal Muscle’. U.S. National Institutes of Health, National Cancer Institute. 02-09-2013 (date of access), <http://training.seer.cancer.gov/anatomy/muscular/structure.html>]

lymph vessels in addition to motor and sensor nerves. Muscle fibers are long tubular structures with diameters in the range $10\text{--}90 \mu\text{m}$ and lengths ranging from several millimeters to several centimeters. Thus the length to diameter ratio for the muscle fibers is high, ranging from 100 to 10,000. In the muscle, several fibers (few to >100 fibers) are arranged in bundles with each bundle surrounded by a layer of connective tissue. In addition, within the bundle, fibers are also surrounded by a network of connective tissue (Fig. 1). The microarchitectural arrangement of the muscle fibers provides a physiological basis for diffusion anisotropy: diffusion of water molecules is facilitated along the long muscle fibers while impeded in the perpendicular plane by the muscle fiber cell walls.

4 Imaging Pulse Sequences for Diffusion-Weighted Magnetic Resonance Imaging

The pulse sequences used to measure the diffusion tensor in muscle are similar to those implemented for the brain (Basser and Jones 2002). They are based on the spin echo, echo planar diffusion-weighted sequence. It should be noted that muscle imaging is challenged by the following characteristics of muscle: low T_2 (32 ms for muscle compared to $70\text{--}80$ ms for brain tissue), low FA (0.2–0.3 for muscle compared to 0.4–0.8 for white matter), and fat infiltration in the muscle (admixture of fat and muscle in a voxel). These considerations have led to sequences with a short TE and efficient fat suppression methods. Approaches to increase SNR include larger voxel sizes, increased averages, and the use of surface coils.

4.1 Spin Echo, Echo Planar Diffusion-Weighted Imaging

The basic physics behind obtaining diffusion-weighted MR images involves the use of two large balanced diffusion gradient sequences, placed around the 180° refocusing pulse (Fig. 2). The first gradient introduces a dephasing of spins that is determined by the magnitude, G , and duration, δ , of the diffusion gradient. The second gradient will completely rephase the phase introduced by the first gradient if the spins are entirely static. The large diffusion gradients and long duration, however, affect the signal from molecules undergoing motion, even on the scale of diffusion-related displacements. Since the sequence is sensitive to these small motions, it is important to acquire the image in very short times in order to freeze all physiological and other motion. This is achieved using an echo planar readout which can acquire a 2D image in ~ 40 –100 ms (echo planar readout not shown in the figure).

The effect of the two diffusion gradient lobes (strength, duration, and diffusion time) is represented by a single term called the “ b -factor” defined as (Basser and Jones 2002):

$$b = \gamma^2 G^2 \delta^2 (\Delta - \delta/3)$$

where the gradient parameters are defined in Fig. 2.

The signal intensity of a diffusion-weighted image, $S(b)$ with respect to the baseline image (all parameters the same but without the diffusion gradient) for the general case of anisotropic diffusion is given by (Basser and Jones 2002):

$$\begin{aligned} \ln\left(\frac{S(b)}{S(b=0)}\right) &= -\sum_{i=1}^3 \sum_{j=1}^3 b_{ij} D_{ij} \\ &= -(b_{xx} D_{xx} + 2b_{xy} D_{xy} + 2b_{xz} D_{xz} + b_{yy} D_{yy} + 2b_{yz} D_{yz} + b_{zz} D_{zz}) \end{aligned}$$

In order to extract the six components, D_{ij} , of the diffusion tensor, diffusion gradients have to be applied in at least six noncollinear directions. When using greater than six directions for the diffusion gradients, there is a tradeoff between number of averages and diffusion gradient directions. The diffusion tensor is diagonalized to obtain the eigenvalues ($\lambda_1, \lambda_2, \lambda_3$) and eigenvectors (v_1, v_2, v_3) of the diffusion tensor ellipsoid. The eigenvector corresponding to the largest eigenvalue has been validated to be along the fiber directions. The eigenvectors define the orientation of the anisotropic diffusion ellipsoid, while the degree of anisotropy is defined by the relative magnitude of the eigenvalues. The “mean diffusivity,” MD, alternately termed as the “apparent diffusion coefficient, ADC,” is the average of the three eigenvalues:

$$MD = \frac{\lambda_1 + \lambda_2 + \lambda_3}{3}$$

FA is a scalar measure of this anisotropy and is derived from the eigenvalues as:

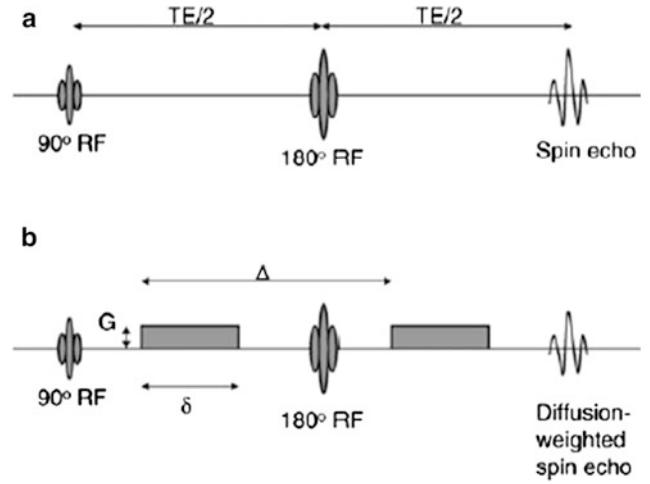


Fig. 2 Diffusion gradient sensitization with a spin echo preparation, the echo planar readout is not shown here. The *top* pulse sequence (a) is used for the baseline acquisition (without diffusion preparation) and the *bottom* pulse sequence (b) includes the diffusion gradient lobes (G) which can be applied along any direction

$$FA = \sqrt{\frac{2}{3}} \sqrt{\frac{(\lambda_1 - \lambda_{av})^2 + (\lambda_2 - \lambda_{av})^2 + (\lambda_3 - \lambda_{av})^2}{\lambda_1^2 + \lambda_2^2 + \lambda_3^2}}$$

FA values range from 0 (isotropic) to 1 (strongly anisotropic). The FA values in muscle are in the range of 0.2–0.3 which is lower than that of white matter (~ 0.5 –0.8). Besides the mean diffusivity and the FA, several scalar measures derived from the tensor have been proposed. These include other measures of anisotropy like the shape of the diffusion: whether it is like a cigar (linear), pancake (planar), or sphere (spherical) (O’Donnell and Westin 2011).

The eigenvectors are conveniently represented in color and the following conventions are used in DTI visualization: with the x -projections mapped to red, y -projections to green, and z -projections to blue. The ultimate goal is to obtain the fiber tracks which represent the physiological unit of the muscle fiber bundles. Several tractography algorithms have been proposed to connect eigenvectors; the most commonly used is known as fiber assignment by continuous tracking, FACT (Mori and van Zijl 2002; O’Donnell and Westin 2011). In this algorithm, the algorithm starts from seed voxels defined by the user or by FA thresholds and follows the eigenvector direction in each voxel. Termination occurs when the FA value falls below a preset threshold or the orientation of the fiber changes by a larger angular threshold. Tract selection (using anatomical ROIs) and seed placement are highly interactive resulting in a strong operator dependence of fiber tracts. Another related approach is streamline tractography which also works by successively stepping in the direction of the principal eigenvector. Several computational methods are used to perform basic streamline tractography: Euler’s method (following the eigenvector or tangent

for a fixed step size) and second order or fourth order Runge–Kutta method (where the weighted average of two or four points is used for each successive step) (Basser et al. 2000). More advanced methods in tractography include probabilistic tractography that provides a measure of the probabilities of connections (Behrens et al. 2003) and tractography using advanced models for fiber crossings (Malcolm et al. 2010). Tractography is an area of active research and a recent review comparing different tractography algorithms is discussed by Lazar (2010). In muscle fiber tracking, FACT and streamline tractography methods have been used in almost all the studies reported so far. Muscle fibers do not cross and present simpler geometrical constructs compared to brain white matter fibers may be one of the reasons for the success of the simpler deterministic algorithms. However, as seen later, muscle tractography is still challenged by the lower FA values, lower SNR as well as the admixture of fat in muscle voxels.

4.1.1 Simulation Studies

Simulation studies have been performed incorporating low T2 values, % muscle fraction, DTI indices (eigenvalues, and FA) typical values for muscle in order to obtain the optimum acquisition parameters and SNR requirements to measure DTI indices with a given accuracy (Damon 2008). In the latter paper, simulations were performed with six standard diffusion gradient directions, and identified the optimum b value to be between 400 and 700 mm^2/s , and SNR of 25 for the baseline image was required to obtain an accuracy of 5 % in the DTI indices when the voxel contained only muscle tissue. The SNR requirements for eigenvector directions were more stringent: $\text{SNR} \geq 25$ and ≥ 45 was required for eigenvector angular deviations of $\pm 4.5^\circ$ uncertainty with muscle fractions of 1 and 0.5, respectively. When considering single voxel angular uncertainty, and $\text{SNR} \geq 60$ was required for $\pm 9^\circ$ uncertainty; this can have consequences for accurate fiber tracking. Froeling also performed simulation studies and determined that at least 12 gradient directions should be employed (Froeling 2012). Increasing the number of gradient directions does increase the accuracy of the eigenvector but it should be balanced by the number of averages so that the acquired diffusion-weighted images are of sufficient image quality to permit image preprocessing (for distortion corrections etc.). A more recent study also considered the effect of fat infiltration/admixture in the muscle and showed that regions must contain at least 76 % muscle tissue to reflect the diffusion properties of pure muscle accurately (Williams et al. 2013). In fat-suppressed diffusion-weighted images, high values of FA were surprisingly found in regions with high % of fat. This was attributed to the lower SNR in these regions which biased the value of the FA. This type of FA bias has been shown in earlier simulation studies focused on the brain as well (Basser and Pajevic 2000).

It should be noted that the optimum b -value for diffusion imaging ($\sim 400 \text{ s/mm}^2$) is lower than that used in the brain ($\sim 1,000 \text{ s/mm}^2$). This allows lower TE values for the sequence which addresses the lower T2 of the muscle. Saupe et al. determined the optimum b -value at 1.5 T for muscle imaging using fiber tracking quality for evaluation; they estimated the optimum value to be 625 s/mm^2 (Saupe et al. 2009). Another important aspect is that most of the DWI/DTI sequences for the brain use a dual 180° pulse (twice refocused) to reduce the effects of eddy current. Most of the muscle DWI/DTI studies reported so far do not use the twice refocused for eddy current correction in order to keep TE at a minimum value. Further, it should be noted that the lower ‘ b ’ values used in muscle DTI do not result in large eddy current artifacts and the smaller eddy current distortions are corrected using post-processing methods.

Typical parameters and scan settings used in spin-echo echo-planar imaging (SE-EPI) based DTI acquisition for the lower leg calf muscles are listed below (Sinha et al. 2011). The acquisition included one baseline and 13 diffusion-weighted images (b factor: 500 s/mm^2) along 13 noncollinear gradient directions. Image acquisition parameters were as follows: Echo Time (TE)/Repetition Time (TR)/Field-of-View (FOV)/matrix: 48 ms/6,400 ms/24 cm/ 128×128 with parallel imaging. Images were reconstructed to a matrix size of 256×256 ; voxel resolution was $0.94 \times 0.94 \text{ mm}$ in-plane resolution (after reconstruction to a 256×256 matrix) with a slice thickness of 5 mm. The sensitivity encoding (SENSE) method was employed in the parallel image reconstruction and a reference scan for coil sensitivity calculation was acquired prior to each DTI acquisition; a parallel imaging reduction factor of two was used. The volume of interest was also shimmed prior to the DTI acquisition. A total of 29–30 slices were acquired contiguously, and six repeats of the acquisition were magnitude averaged for a total scan time of 9 min. A spatial spectral fat-saturation pulse was used to suppress the fat signal.

4.2 Stimulated-Echo Planar Diffusion-Weighted Imaging

The overwhelming number of muscle DTI studies have used the spin echo EPI diffusion-weighted imaging. A few studies, however, have used the stimulated echo sequence since it permits diffusion weighting at small values of TE; as explained earlier, the latter is advantageous since muscle T2 is low. In this method, three 90° pulses are applied: the first diffusion lobe is applied between the first two 90° pulses and the balancing diffusion gradient is applied after the third 90° pulse (Fig. 3). The time between the second and third 90° pulse (\sim the diffusion time) can be fairly long as the magnetization is stored longitudinally (Fig. 3). Thus for the same

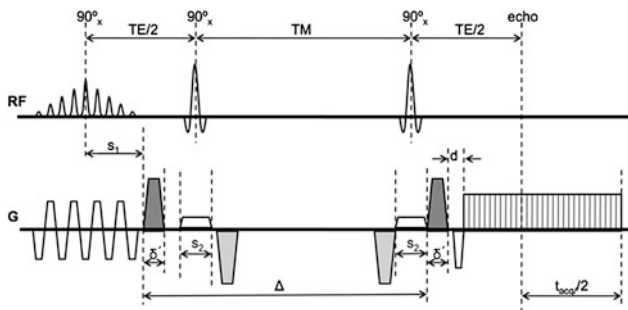


Fig. 3 Schematic of eddy-current compensated stimulated-echo prepared DW-EPU pulse sequence. Diffusion weighting gradients are in *black* and eddy current compensating gradients are in *gray* [Reprinted with permission from Karampinos et al. (2012)]

'*b*' value in SE and STE, the gradient strength and duration can be smaller since the diffusion time, delta, can be made fairly large. The TE of the STE sequence depends on the time between the first two 90° pulses: this can be made much smaller than the SE analog. However, the SNR of the STE signal is reduced by half compared to an SE signal and this affects the overall image quality. Schwenzer et al. studied the variation of muscle diffusion indices with flexion using an STE-EPI sequence (Schwenzer et al. 2009). More recently, Karampinos et al. combined eddy-current compensated diffusion-weighted stimulated-echo preparation with sensitivity encoding (SENSE, reduction factor 2.86) to obtain high SNR and to reduce the sensitivity to distortions and T(2)* blurring in high-resolution skeletal muscle single-shot DW-EPI (Karampinos et al. 2012). The rather high reduction factor of 2.86 certainly reduced distortions and fat-water mismapping artifacts, but also contributes to a loss in SNR. They were able to obtain voxel resolutions of 17 mm³ which is of the order achievable with single-shot SE-EPI DW imaging. The TE (31 ms) is lower than that possible with SE-EPI (~42–49 ms) but is still not low enough to compensate for the loss in signal intensity by a factor of 0.5 in a STEAM acquisition. The few studies, so far, have not convincingly demonstrated that STE diffusion preparation offers a distinct advantage over the SE diffusion preparation (note: parallel imaging has been used with both techniques to reduce the distortion/fat mismapping artifacts). A recent clinical study uses STE diffusion preparation to study Chronic Exertional Compartment Syndrome (CECS) of the Lower Leg Muscles (Sigmund et al. 2013).

5 Post-processing of Diffusion-Weighted Images

Echo planar diffusion-weighted images suffer from low signal-to-noise and from geometric distortion artifacts arising from eddy currents as well as from B₀ field

inhomogeneities. Several groups have adapted denoising and correction techniques originally developed for brain images to muscle DTI data.

5.1 Denoising

Froeling et al. have used a Rician linear minimum mean square error (LMMSE) noise suppression algorithm on the diffusion-weighted images and obtained visually improved images (Froeling et al. 2012; Aja-Fernandez et al. 2008). Sinha et al. evaluated log-Euclidean anisotropic filter available from the software package, MedINRIA (Sinha et al. 2011; Sinha and Sinha 2011; Arsigny et al. 2006). The latter is a tensor smoothing algorithm and is based on first transforming to the matrix logarithm L of a tensor D : $L = \log(D)$, and running computations on L . Smoothing is then performed on L to obtain \tilde{L} from which the regularized tensor is obtained by taking the matrix exponential: $D = \exp(\tilde{L})$. The standard deviation of the lead eigenvector orientation reduced with the smoothing (average standard deviation of orientation in the original images: $3.1 \pm 2.5^\circ$ and in the denoised tensor images: $1.01 \pm 0.6^\circ$) and this difference was also significant (paired 2-tailed, t test, $p = 0.001$). Figure 4 shows eigenvector images of the lower calf before and after denoising; the smoothing of the fiber orientation can be readily appreciated. Incorporation of noise reduction methods for muscle DTI clearly improves SNR and should be employed if fiber tractography is the end goal. A recent study reported a denoising algorithm tailored to muscle diffusion tensor data (Levin et al. 2011). A key feature of the algorithm is that it performs denoising of the lead eigenvector field simultaneously with its extraction from the noisy tensor field. This allows the vector field reconstruction to be constrained by the architectural properties of skeletal muscles. The latter algorithm shows promise and needs large-scale testing; however, it does require some a priori knowledge of fiber architecture to impose constraints on the denoising algorithm. Additional studies need to be undertaken to compare and customize the different denoising algorithms available and also to determine if the raw diffusion-weighted images or the tensor should be denoised in terms extent of noise reduction and impact on FA values.

5.2 Geometric Distortions from Eddy Currents and Motion

The diffusion-weighted images have geometric distortions from eddy currents arising from the large diffusion gradients (Sinha et al. 2011; Sinha and Sinha 2011; Heemskerk et al. 2010; Froeling et al. 2012). This distortion and motion

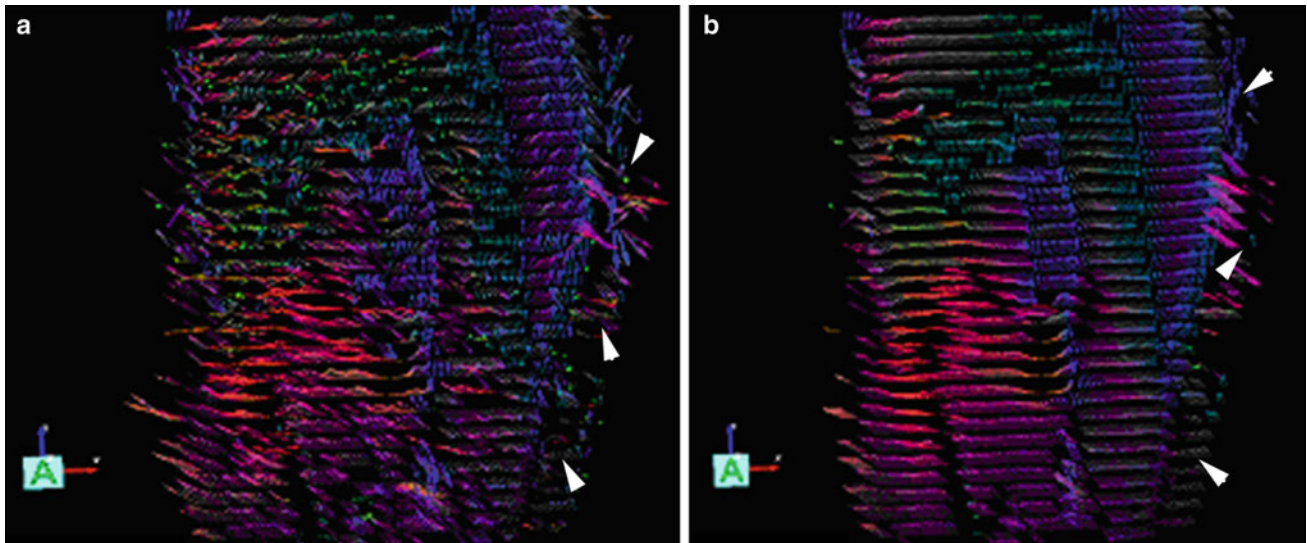


Fig. 4 The leading eigenvector is shown in both images as *arrows* with the color indicating vector direction with the following color map (*blue* superior-to-inferior direction, *red* medial to lateral direction, and *green* anterior to posterior direction). The *left image (a)* is unsmoothed and the *right image (b)* is the corresponding smoothed image. Large

eigenvectors outside the muscle (indicated by *white arrowheads*) correspond to fat regions and show erroneous fractional anisotropy and eigenvector directions [Reprinted with permission from Sinha et al. (2011)]

correction is performed by an affine transform to the baseline image volume of the diffusion-weighted data. The affine transformation is used to reorient the *b*-matrix as well (Leemans and Jones 2009).

5.3 Geometric Distortions from Susceptibility Artifacts

This artifact arises from magnetic field inhomogeneities primarily due to susceptibility differences in adjacent structures. The field inhomogeneities result in a spatial mis-mapping with regions of signal loss and signal pile-up. The extent of distortions is the same in the baseline and in the diffusion-weighted images. Most muscle DTI studies do not correct for this artifact. However, it is important to correct for these geometric distortions in order to perform accurate fiber tractography, correlate morphological to diffusion tensor data, and to enable image-based modeling. Methods used in brain diffusion tensor imaging have been extended to muscle diffusion data. One method that has been implemented is based on acquisition of phase images which map the field inhomogeneity; these phase values can be used to directly assign voxels to the correct location (Froeling 2012; Froeling et al. 2012). This approach, however, requires an additional double echo gradient echo scan and it is not clear if it will work when parallel imaging is used. An alternate approach is to nonlinearly deform the baseline image of the diffusion-weighted dataset to a

geometrically accurate structural image and apply the deformation to the diffusion tensor calculated from the uncorrected data (Sinha et al. 2011; Sinha and Sinha 2011). Figure 5 shows the axial slice of the lower leg from the baseline diffusion-weighted image as acquired and the same image after correction with a nonlinear deformation algorithm. The nonlinear deformation was applied to the diffusion tensor rather than to the diffusion-weighted images so that appropriate tensor reorientation can also be performed. The better geometrical match of the corrected data to the structural images can be readily appreciated by the better match of the contours.

6 Muscle Model of Diffusion

Tseng et al. analyzed diffusion tensor data in myocardial muscle and concluded that the eigenvectors corresponding to the leading, second, and third eigenvalues correspond to the directions along the long axis of the fibers, parallel to the myocardial sheets, and normal to the sheets (Tseng et al. 2003). This myocardial muscle model has been confirmed by histological examination as well (Scollan et al. 1998). Damon et al. were the first to confirm that the pennation angle of the lateral gastrocs fibers in a rat model estimated from DTI is close to that measured by direct anatomical inspection, DAI (Damon et al. 2002). However, the anatomical correlates of the second and third eigenvector of muscle fibers have not yet been conclusively established.

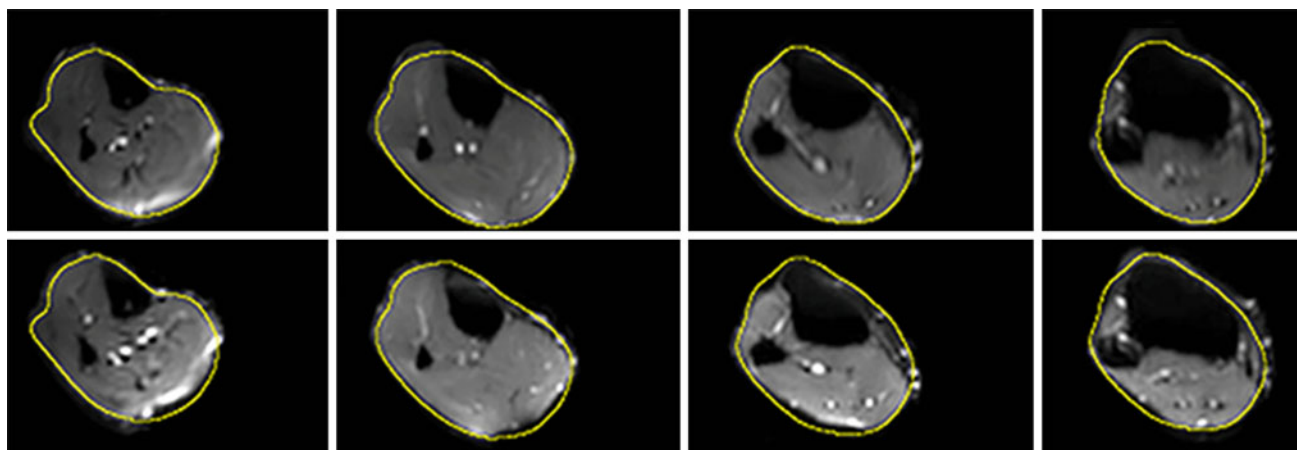


Fig. 5 *Top row* Corrected baseline images after nonlinear deformation to an image volume acquired using a gradient echo sequence with fat saturation. *Bottom row* Original baseline images of the diffusion-weighted series. The *yellow* contour superposed on both image

volumes was obtained from the corresponding slice in the gradient echo image. The improvement in geometric fidelity is clearly apparent by a comparison of the contour matching for the two sets

Galbán et al. were the first to suggest a model to explain the observed diffusion tensor eigenvalues in skeletal muscle (Galbán et al. 2004). They proposed that since the lead eigenvector was along the long axis, the second and third eigenvectors are in a plane orthogonal to the long axis. The second eigenvector is hypothesized to run along the sheets of individual muscle fibers within the endomysium, the region between the fibers. The eigenvector associated with the third eigenvalue is then related to transport pathways with the muscle in this model. They verified the model prediction that PCSA is proportional to the third eigenvalue in the lower leg muscles.

An extension of this model was advanced to account for gender-based differences in DTI indices: the extended model includes the muscle fiber volume fraction in a well-defined arbitrary muscle volume (Galbán et al. 2005). The extended model predicts that a larger volume fraction of skeletal muscle in males is muscle fibers (anisotropic hindered diffusion) compared to females who have a larger fraction of endomysium (isotropic, less hindered diffusion); this was verified in their study as females had a larger ADC values while males had higher FA values (Galbán et al. 2005).

Karampinos et al. proposed an interesting diffusion tensor model which took into account the cross-sectional asymmetry of muscle fiber geometry (Karampinos et al. 2007, 2009). In their model, diffusion occurs in a space composed of the space within the muscle fiber and the extracellular space. The muscle fibers themselves were modeled as cylinders of infinite length with an elliptical cross-section with dimensions derived from histological studies of excised muscle. In the model, λ_2 and λ_3 (the second and third eigenvalues) reflect the principal diameters of the elliptical cross-sectional area of the myofibrils.

Though there is no complete validation as yet for the second and third eigenvector directions, the elliptical cross-sectional model has some support since the second eigenvector has been tracked in a recent study (Gharibans et al. 2011).

It is also possible to infer the link between the eigenvalues and the fiber microarchitecture by looking at changes on flexion. Consistent changes have not been reported for plantarflexion, but most studies show that λ_3 increases. This is in line with the models relating λ_3 to muscle diameter. In the elliptical cross-sectional model, if there is isotropic deformation in the fiber cross-section, similar increases in λ_2 should be expected. However, evidence from other studies such as strain rate tensor (Englund et al. 2011; Sinha et al. 2012), show that fiber cross-sectional deformation is highly anisotropic. This suggests that if deformation is only along one direction, λ_2 should not change as much as λ_3 . Experimental evidence of small changes in λ_2 with flexion comes from Hatakenaka et al. (2008) and Sinha et al. (2011). However, other studies have reported both decreases and increases in λ_2 (Deux et al. 2008). More studies using robust acquisition and post-processing techniques are required to document changes in the diffusion indices with flexion; such studies may help elucidate the diffusion model in the musculoskeletal (MSK) system.

7 Diffusion Tensor Indices in the Normal MSK System

Detailed analysis of the DTI of the forearm muscles have been reported by Froeling et al. (2012). The eigenvalues, MD, and FA were calculated for six muscles of the forearm

as well as for the whole muscle volume. Typical values for the MD in the whole muscle of the forearm were $1.49 \pm 0.09 \times 10^{-9} \text{ m}^2/\text{s}$ and FA values were 0.30 ± 0.02 . Values reported for the MG of the lower leg are $1.32 \pm 0.06 \times 10^{-9} \text{ m}^2/\text{s}$ and FA values were 0.23 ± 0.04 (Sinha and Sinha 2011). The same group also extracted the diffusion indices for the different compartments of the soleus (Sinha et al. 2011): MD and FA of posterior soleus: $1.47 \pm 0.06 \times 10^{-9} \text{ m}^2/\text{s}$ and 0.20 ± 0.04 ; MD and FA of anterior soleus: $1.60 \pm 0.08 \times 10^{-9} \text{ m}^2/\text{s}$ and 0.20 ± 0.04 . Heemskerk et al. reported the values in anterior tibialis (TA) for the mean diffusivity as $1.64 \pm 0.05 \times 10^{-9} \text{ m}^2/\text{s}$ and for the FA as 0.23 ± 0.04 (Heemskerk et al. 2010). Heemskerk et al. also determined the coefficient of variation (CV) for the diffusion indices, fiber orientation, and lengths. They report CV of $<3\%$ for the eigenvalues and MD, $<8\%$ for the FA, and the repeatability coefficients of the fiber pennation angle and length to be less than 10.2 and 50 mm, respectively. The above measurements of normal diffusion indices in skeletal muscle were performed at 3 T. A comparison of 1.5 and 3 T scanners based on two subjects scanned on 3 days to calculate the coefficient of variability (CV) showed that the values for the DTI indices as well as for the fiber orientation were in a similar range ($<3\%$ for the eigenvalues, $<8\%$ for the FA, and 8–12% for the fiber orientation). Given the widespread availability of 1.5 Tesla scanners, this opens the possibilities for using DTI to monitor muscle architecture in normal and diseased states (Sinha and Sinha 2011).

The repeatability studies allow one to determine if the measurement precision is sufficient to detect changes with disease state. DTI indices are known to change in the range of 10–20% in diseased or damaged tissue (Heemskerk et al. 2006, 2007; Qi et al. 2008). The RC of the DTI indices (eigenvalues, FA) in the lower leg muscles is reported to be less than 10%, and thus the DTI sequences should be capable of detecting changes in muscle DTI indices with disease/damage. Changes in muscle architecture arising from changes in ankle positions or from contraction can be as small as 3–5°, so that repeatability coefficients for fiber orientations should be in this range. The average RCs of the fiber orientations in prior reported studies is $\sim 8^\circ$, which is more than the anticipated changes in fiber orientation with ankle position or from contraction. However, it should be noted that muscle architecture changes are typically monitored without any change in patient position, so that these measurements (same session, no subject repositioning) will have a higher reproducibility than that measured on separate days with subject repositioning. This is probably the reason that fiber orientation changes of the order of 8° could be detected even when the RC value was in the same range (Sinha et al. 2011; Sinha and Sinha 2011).

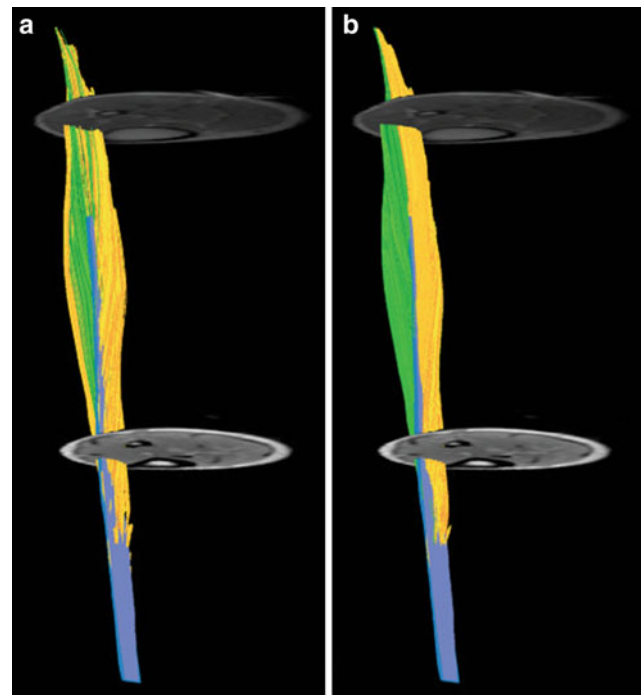
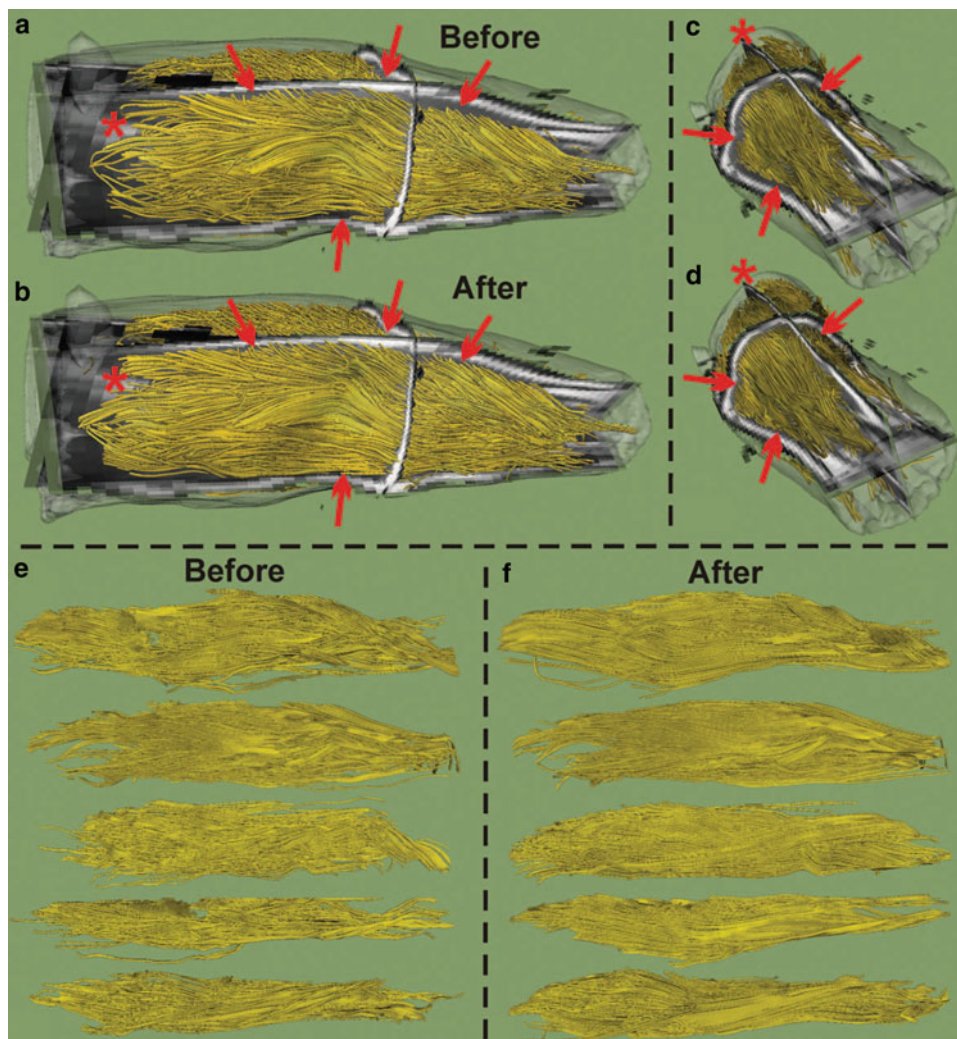


Fig. 6 Fiber trajectories for subject three before (a) and after (b) quantitative assessment. Note the yellow fibers in both compartments in a. The aponeurosis is indicated in blue and fibers originating from the deep aspect of the aponeurosis are indicated in shades of yellow, while fibers originating from the superficial aspect of the aponeurosis are indicated in shades of green. Color variations within the tracts exist only for contrast [Reprinted with permission from Heemskerk et al. (2009)]

7.1 Diffusion Tensor Imaging Under Passive and Active Muscle Contraction

There have been varying reports on the changes under passive and active muscle contraction. Hatakenaka reported that in the medial gastrocnemius (mGM) passive contraction resulted in a decrease in λ_1 , no change in λ_2 and an increase in λ_3 which lead to a lower FA value (Hatakenaka et al. 2008). The opposite effect was seen in the TA. Duex et al. reported that in the mGM, the three eigenvalues and ADC increased while FA decreased during an active contraction from neutral to plantarflexion (Deux et al. 2008). The reverse trend was observed in the TA. Okamoto et al. also performed DTI under active contraction and found higher values for λ_1 and λ_2 as well as FA in the mGM with an opposite effect for the TA and attributed some of the changes to changes in focal temperature and perfusion (Okamoto et al. 2010). Schwenzler et al. measured orientation changes in the soleus under neutral and plantarflexed ankle positions (Schwenzler et al. 2009). For the soleus, they report increase in λ_2 and λ_3 , no change in λ_1 , a decrease in FA, and a small change of 4° in the fiber orientation with respect to the z-axis. Sinha et al. report much larger changes in the soleus

Fig. 7 Fiber tractography of the whole human forearm. Muscle fibers are shown on *top* of orthogonal cross-sections and surface renderings of the T1-weighted images. **a**, **c** Tractography before displacement and diffusion tensor shear corrections. **b**, **d** Tractography after corrections. Regions where T1-weighted data and fiber tracts were severely misregistered are indicated with *red arrows*. After postprocessing the misregistration virtually disappeared and denser fiber tracking continued toward the proximal end of the forearm as indicated by the *red asterisk*. **e**, **f** Segmented Flexor digitorum profundus of all five subjects before (**e**) and after (**f**) postprocessing [Reprinted with permission from Froeling et al. (2012)]



when the foot is in the neutral and plantarflexed states ($\sim 60^\circ$ in the posterior soleus) (Sinha et al. 2011).

Hatakenaka have built on diffusive models in skeletal muscle in the literature to propose a model for contraction (Hatakenaka et al. 2008). Sarcomeres ($2\ \mu\text{m}$ length) are shortened on contraction, while muscle fiber cross-sectional diameter ($40\text{--}120\ \mu\text{m}$), as well as that of myofibrils ($3\ \mu\text{m}$), increase. Since myofibril dimensions are of the order of the observed diffusion lengths ($10\ \mu\text{m}$), the diffusion in the radial direction increases due to increase in myofibril diameter; this is confirmed by observations on λ_3 . Hatakenaka also suggested that sarcomere shortening may contribute to a decrease in λ_1 (Hatakenaka et al. 2008). Other models propose that λ_1 should not change with contraction as whole muscle fiber lengths are far greater than diffusion lengths, resulting in λ_1 being insensitive to muscle fiber length changes (Schwenzer et al. 2009). The increase in λ_3 seen in several studies can be attributed to an increase in

muscle fiber diameter as the muscle contracts on plantarflexion. However, both experimental data and models are not consistent and more studies on flexion may help identify consistent changes in diffusion indices and may ultimately provide clues to the correct diffusion model.

8 Fiber Tractography

The ultimate aim of muscle DTI is tracking the muscle fibers to determine the microarchitecture: pennation angles, fiber lengths, and curvature. Damon et al. showed that fibers tracked in rat muscle at 4 T correlated well with direct anatomic imaging (Damon et al. 2002). Sinha et al. reported some of the earliest fiber tractography in human in vivo calf muscle (Sinha et al. 2006). They showed the feasibility of fiber tracking in several muscle compartments of the in vivo calf muscle. Lansdown et al. established an automated

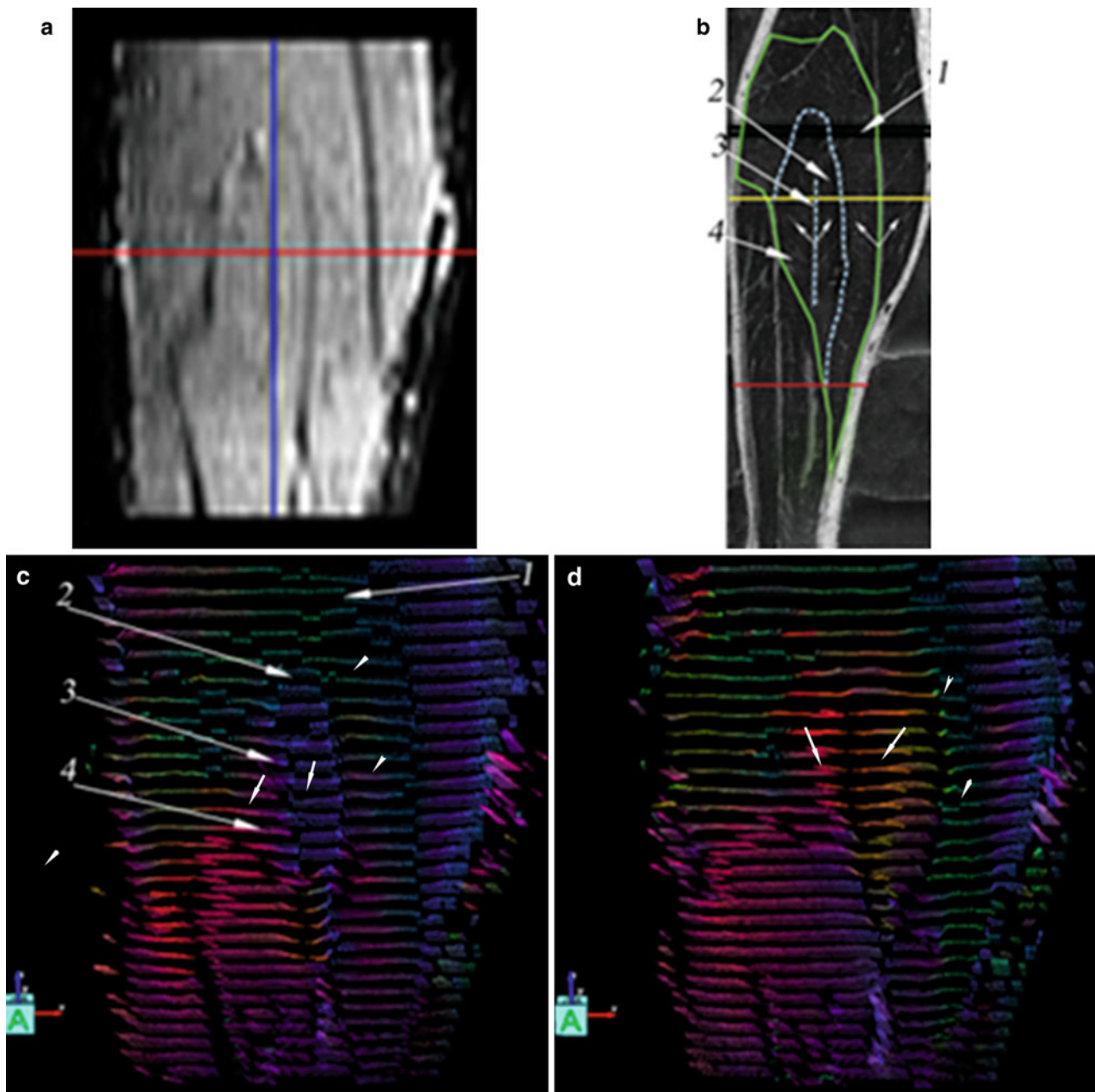


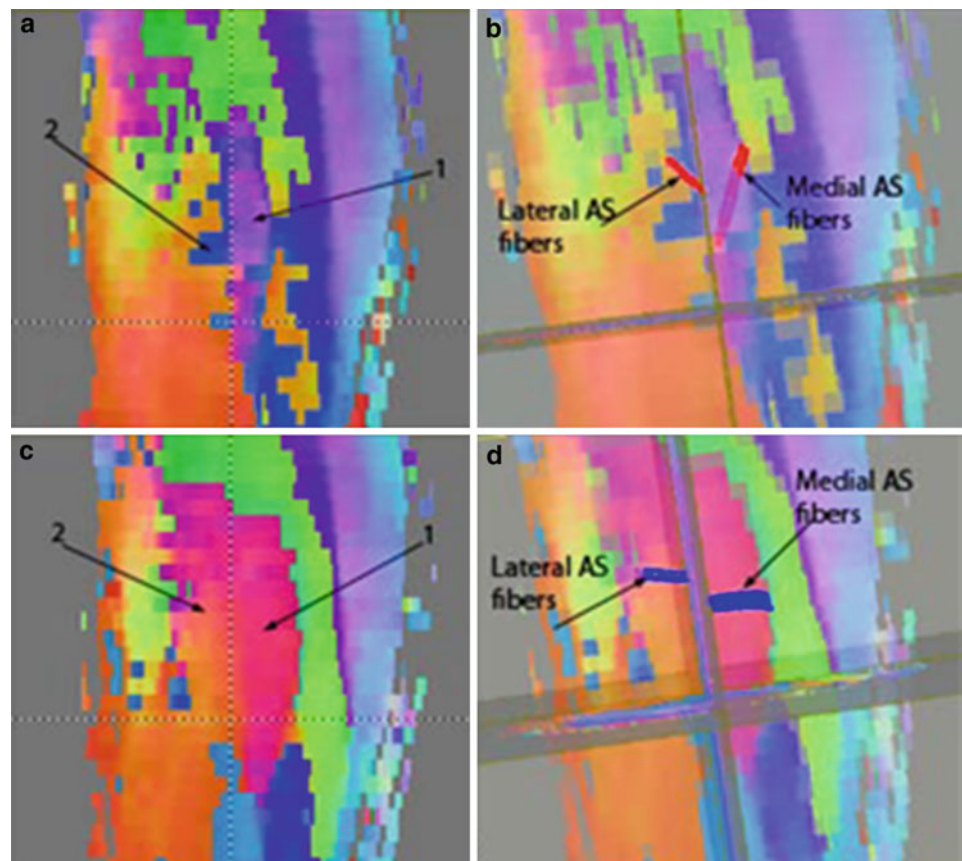
Fig. 8 Coronal view of the soleus. The coronal morphological image at rest (**a**), an image at a approximately corresponding location from the Visible Human dataset (**b**), leading eigenvector images corresponding to the coronal morphological image at rest (**c**), and in plantarflexion (**d**). In the Visible Human image (**b**), the soleus is outlined in *solid green*, the *blue dotted lines* correspond to the anterior soleus. The compartments identified in the visible human are posterior soleus (*arrow 1*), the medial anterior soleus (*arrow 2*), the median

septum (*arrow 3*), and the lateral anterior soleus (*arrow 4*). These compartments are also identified on the eigenvector image at rest (**c**) with the same arrow labels as in **b**. On plantar flexion there are large fiber orientation changes in both compartments of the anterior soleus and in the posterior soleus visualized as a change of colors in **d**. *Short arrowheads* (*solid* for posterior soleus and *unfilled* for anterior soleus) indicate the respective regions in the rest and plantarflexed state)

method for fiber tracking; in their approach, seed points were not manually placed (as in most other fiber tracking studies) but were automatically generated from the aponeurosis surface for the muscle of interest (Lansdown et al. 2007). They determined pennation angles automatically from seed

points close to the aponeurosis of origin for the deep and superficial compartment of the TA. They report that the pennation angle decreased from 16.3° (SD: 6.9) to 11.4° (SD: 5.0) along the muscle's superior-to-inferior direction. The mean value of the pennation angle was greater in the

Fig. 9 Coronal color map of the lead eigenvector at neutral (a) and at plantar flexion (b) with arrows showing the anterior soleus medial and lateral subcompartments (arrows 1 and 2, respectively) separated by the median septum. A vertical dotted line is placed at the location of the median septum. Fibers (in red for neutral and in blue for plantarflexed ankle positions) tracked from seed points located in the lateral and medial subcompartments of the anterior soleus in the neutral (c) and in the plantarflexed positions (d). Fiber colors are assigned by the user so as to maximize the contrast with the underlying eigenvector images



deep than in the superficial compartment. In an extension of this work, Heemskerk et al. used quantitative criteria to assess fiber tracking in the deep and superficial compartments of the TA (Heemskerk et al. 2009). Quantitative criteria for fiber tracking included the presence and similarity of fibers to neighboring tracts, length of fibers including only those that terminated close (within two voxels) to the muscle border (Fig. 6). They also evaluated SNR requirements and optimized the fiber tracking parameters including termination criteria of FA ($0.15 < FA < 0.75$) and curvature ($<45^\circ$). They conclude that SNR levels of 106 and 147 in the superficial and deep compartments were sufficient for generating fibers that covered $89.4 \pm 9.6\%$ and $75.0 \pm 15.2\%$ of the aponeurosis area in the superficial and deep compartments, respectively. A more recent paper by the same group deals with the reproducibility of fiber tracts in the TA (Heemskerk et al. 2010). They determined that while the repeatability of the diffusion indices (MD, FA, eigenvalues) is very good, the repeatability of the architectural measurements (pennation angle and fiber length) is acceptable. This emphasizes the fact that fiber tracking is challenging and extraction of quantitative architectural parameters should be approached with a robust acquisition scheme (high SNR, good fat suppression, low distortions) and rigorous post-processing algorithms.

The importance of optimized image acquisition and post-processing to reduce noise, correct for eddy current, and susceptibility-induced distortions has also been emphasized by Froeling et al. (2012). The latter study showed that significant improvements in forearm fiber tracking as well as in diffusion indices resulted from the post-processing corrections. They employed several post-processing steps including signal-to-noise improvement by a Rician noise suppression algorithm, image registration to correct for motion and eddy currents, and correction of susceptibility-induced deformations using magnetic field inhomogeneity maps. Fibers were generated using a custom built tool, the DTITool program (<http://bmia.bmt.tue.nl/software/dtitool>) from 1 to 5 seeding ROIs per muscle (van Aart et al. 2011). The angular change per integration step was limited to $<5^\circ$ per step, which restricts fiber curvature rather severely. Figure 7 shows the marked improvements in fiber tractography with the implementation of the post-processing tools.

Sinha et al. reported on the complex architecture within the soleus; this study also identified the potential for DTI studies to map fibers under rest and plantarflexion conditions (Sinha et al. 2011). It should be noted that compared to the TA and the muscles of the forearm, the soleus architecture is much more complex and presents additional challenges in fiber tracking. The soleus has posterior and anterior

Fig. 10 Sagittal color map at rest (a) and at plantar flexion (c) with arrow showing the posterior soleus. The color maps show that the posterior soleus has a stronger anterior–posterior orientation at plantarflexion. Fibers (in blue) tracked from seed points located along the length of the posterior soleus run anterosuperior to posteroinferior in both rest (b) and plantarflexion (d); in the latter the fibers are shorter with larger pennation angles (d)

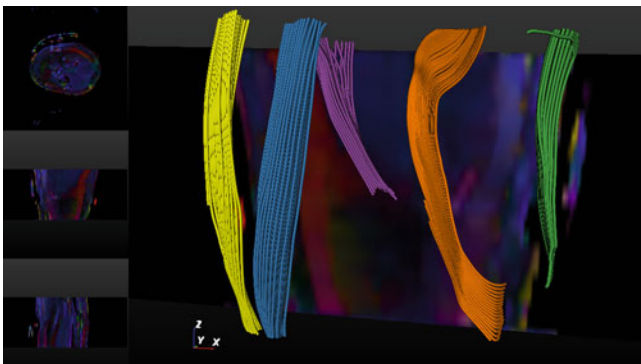
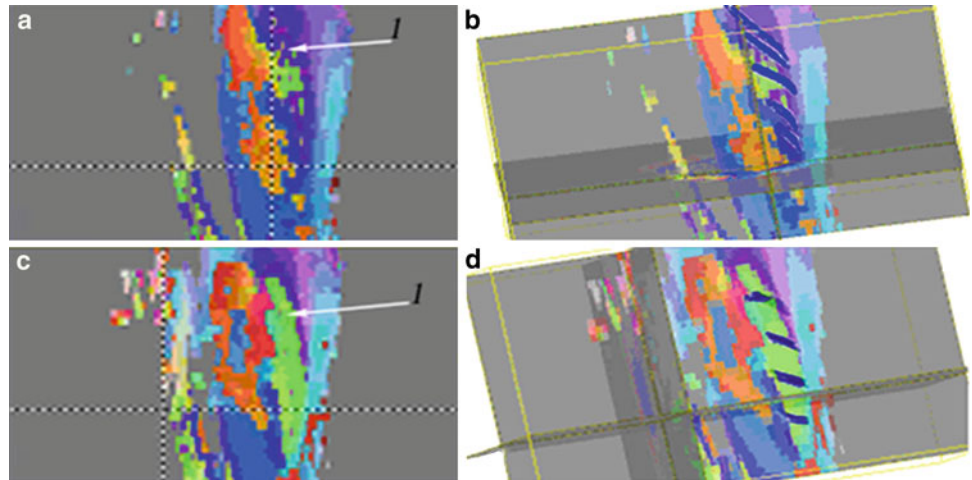


Fig. 11 Fibers tracked from seed points in each muscle compartment using DTITool. Fibers in each compartment are shown in different color to facilitate visualization. Fibers are overlaid on the color FA map to provide an anatomical reference. Fibers are colored as follows: yellow (superficial anterior tibialis), blue (deep anterior tibialis), purple (lateral gastrocnemius), brown (soleus), green (medial gastrocnemius)

compartments; 3D cadaveric analysis had shown that the anterior soleus is bipennate with the fiber bundles joining the median septum and the anterior aponeurosis (Agur et al. 2003). Figure 8 shows lead eigenvector DTI images from the soleus under rest and plantarflexion states. A qualitative comparison to the 3D cadaveric analysis by Agur et al. identifies three muscle compartments: posterior, anterior, and marginal soleus (Agur et al. 2003). The eigenvector directions and compartments from the DTI data (Fig. 8) agreed with the fiber directions inferred earlier using the Visible Human dataset by Hodgson et al. (Hodgson et al. 2006). In the latter paper, fibers were identified indirectly from the direction of the fascicles and can thus be only considered as rough indicators of fiber direction. Agur et al. identify the posterior soleus fiber bundles as attaching to the posterior surface of the anterior aponeurosis and to the anterior surface of the posterior aponeurosis. The fiber bundles are directed from anterosuperior to posteroinferior. This

direction is confirmed in the eigenvector images (Fig. 8). Agur et al. also identify the anterior soleus as bipennate where the fiber bundles join the median septum and the anterior aponeurosis (Agur et al. 2003). The median septum is a tapering vertical sheet of aponeurosis with fiber bundles attaching to the medial and lateral surfaces and directed superomedially and superolaterally. The bipennate structure, the median septum as well as the superomedial and superolateral directions of the anterior soleus are confirmed by the eigenvector visualization (Fig. 8) and the fiber tracts (Fig. 9). Fiber tracking in the compartments in the posterior soleus under rest and plantarflexion are shown in Fig. 10. In both the anterior and posterior soleus, fiber orientation changes are such that fibers oriented primarily along the proximal–distal (superior–inferior) directions in the neutral position change to either a medial–lateral (anterior soleus) or an anteroposterior (posterior soleus) direction. As the aponeurosis runs approximately parallel to the proximal–distal direction, the directional change seen in both the posterior and anterior soleus translates to larger pennation angles.

Figure 11 shows fiber tracks generated in all the lower calf muscles using DTITool. The diffusion tensor was smoothed using a log anisotropic diffusion filter prior to tracking and post processing included eddy current and motion correction algorithms. This figure shows that with optimized image acquisition and post-processing methods, robust delineation of fibers is possible.

8.1 Fiber Pennation Angles and Fiber Lengths

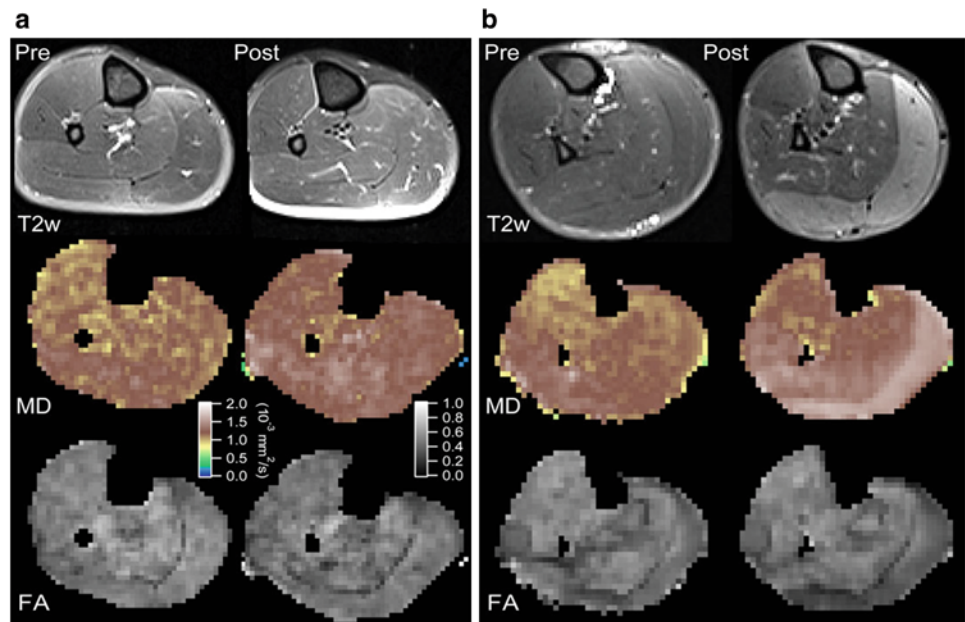
The report by Heemskerk et al. is a comprehensive evaluation of fiber lengths and pennation angles (Heemskerk et al. 2009). They divided the aponeurosis surface of the deep and superficial compartments of the TA into 15 segments and reported the average values of the fiber lengths and pennation angles in each segment. Fiber lengths ranged

Table 1 Reproducibility of medial gastrocnemius fiber architecture at 1.5 T

	Fiber length (mm)		X (°)		Y (°)		Z (°)	
	N	PF	N	PF	N	PF	N	PF
Mean	44.56	29.86	79.88	71.78	99.88	98.40	16.13	26.33
STD	3.71	5.26	2.24	5.94	3.69	4.80	3.58	5.68
CV-av	6.34	10.35	2.80	8.20	3.94	4.78	22.59	16.57
RC-av	7.68	8.83	6.19	16.27	10.92	12.98	10.18	12.69

Reprinted with permission from Sinha and Sinha (2011)

Fig. 12 T2-weighted MRI and DTI in a healthy volunteer (a) and a CECS patient (b). Right calf muscle before (pre) and after (post) treadmill exercise [Reprinted with permission from Sigmund et al. (2013)]



from 60 to 120 mm in the superficial compartment with longer fiber occurring more distally and the pennation angle (18–20°) peaked in the mid-portion along the length of the TA. Similar patterns were seen for the deep compartment of the TA with the exception of the pennation angle which had the lowest value in the mid-section of the muscle.

Sinha et al. report a preliminary estimate of fiber lengths (averaged over three subjects) in the neutral and plantarflexed positions for the soleus: posterior soleus: 21.8 ± 2.7 mm (neutral) and 17.7 ± 3.1 mm (plantarflexed); anterior medial soleus: 19.31 ± 3.4 mm (neutral) and 20.04 ± 2.9 mm (plantarflexed); anterior lateral soleus: 10.69 ± 2.6 mm (neutral) and 14.47 ± 2.8 mm (plantarflexed). As anticipated, the posterior soleus fibers decrease in length on contraction. However, the changes in the anterior soleus are contradictory as the fiber length increases on contraction. This can be explained by the fact the anterior soleus cross-section increases (at the location where the fibers were tracked) in the plantarflexed ankle position (Fig. 8). The soleus fiber lengths in the neutral and

plantarflexed positions from this study are lower than that reported by Martin et al. using ultrasound measurements (Martin et al. 2001). One reason advanced by the authors for lower fiber lengths is that a very low threshold was set for angular changes of successive fiber orientations to prevent fibers being tracked across the different muscle subcompartments. This low threshold may have prevented fibers from tracking across voxels with even moderate changes in curvature, leading to shorter fiber lengths.

Sinha et al. have also reported on fiber architecture for the mGM, MG in the neutral and plantarflexed state (Sinha and Sinha 2011). They found fiber tracking to be most robust from seed points positioned (on coronal images) 45–55 mm from the most distal aspect of the MG and just adjacent to the aponeurosis of insertion in a coronal view. Seed voxel selection influenced fiber lengths more than the fiber orientation since many seed voxels lead to early termination of correctly oriented fibers. This was true especially for the most distal regions of the MG. The mean fiber length and fiber orientation of the tracked fibers in the MG

(Table 1) compare well with the ultrasound measurements on MG fiber length and pennation angles in the relaxed and contracted state (Muramatsu et al. 2002). The latter study reported the fiber length in the relaxed/contracted state as 43.6 ± 8.6 mm/ 27.7 ± 5.6 mm which is comparable to the values in Table 1.

9 Diffusion-Weighted and Diffusion Tensor Imaging in Muscle Injury

DWI and DTI have been used to monitor muscle injury in animal models and humans. Bley et al. have a recent review on diffusion-weighted imaging applied to MSK trauma, tumors, and inflammation (Bley et al. 2009). Line scan diffusion imaging of denervated rat muscle showed the potential of early detection of peripheral nerve injury before changes can be detected on T2 weighted MRI or electromyography (Yamabe et al. 2007). Heemskerk et al. have monitored dynamic changes in T2 and DTI indices after femoral artery ligation (Heemskerk et al. 2007). ADC increased immediately after ischemia was induced and then recovered to baseline values as muscle regeneration occurred. DTI was also performed on healthy and dystrophic skeletal muscle after lengthening contractions on mouse models at 7 T. The latter study found greater increases in ADC and decreases in FA in dystrophic than normal muscle which reflected the larger loss in torque in the dystrophic muscle (McMillan et al. 2011). Esposito et al. recently reported that multiparametric MRI can be used to monitor inflammatory and structural muscle changes in mice models (7 T); increases in T2 and FA were observed in response to inflammatory infiltration and muscle regeneration in the transient response of the tissue to acute injury and in age-related sarcopenia (Esposito et al. 2013).

ADC and FA have been shown to increase after lengthening contractions in human skeletal muscle (Nakai et al. 2008). Zaraiskaya et al. were one of the first to report on DTI evaluation of human muscle injury. They reported an increase in ADC and marked decrease in FA in the soleus and gastrocnemius muscles after calf muscle injury (Zaraiskaya et al. 2006). A recent report showed that DT-MRI (ADC and FA) can detect changes in muscle structure after eccentric exercise; DTI changes correlated with histological indices obtained by muscle biopsy (Cermak et al. 2012). The utility of DWI in monitoring inflammatory myopathies has also been reported (Qi et al. 2008). Sigmund et al. recently reported DTI measurements in CECS of the Lower Leg Muscles; they found that all diffusivities significantly increased ($P < 0.0001$) and FA decreased ($P = 0.0014$) with exercise (Fig. 12). In normal

the increase in MD was significantly less than that in subjects with CECS (Sigmund et al. 2013).

10 Conclusion

Diffusion-weighted and diffusion tensor imaging of the muscle are emerging as potential tools to characterize muscle structure and relate to functional status. The methodology to extract diffusion indices is now well established and has been shown to have sufficient reproducibility to track changes that occur with disease states. There have been relatively few applications of this powerful method in the clinical setting. However, the technology is mature enough for application to monitor conditions such as sarcopenia, compartmental syndrome, myopathies, and disuse atrophy.

While diffusion indices can be extracted rather reliably, fiber tracking is a more challenging task. In order to establish fiber architecture from diffusion tensor imaging on a clinical footing, more large-scale studies on reproducibility of these parameters needs to be established. This will include further technical improvements in acquisition and in postprocessing. However, many of the tools are already available and a focused effort at establishing the guidelines for tractography may enable clinical studies using this method. In summary, DWI and DTI of muscle open a range of possibilities for assessing muscle structure and its changes with normal aging and in disease conditions.

References

- Agur AM, Ng-Thow-Hing V, Ball KA, Fiume E, McKee NH (2003) Documentation and three-dimensional modeling of human soleus muscle architecture. *Clin Anat* 16:285–293. doi:[10.1002/ca.10112](https://doi.org/10.1002/ca.10112)
- Aja-Fernandez S, Niethammer M, Kubicki M, Shenton ME, Westin CF (2008) Restoration of DWI data using a Rician LMMSE estimator. *IEEE Trans Med Imaging* 27:1389–1403. doi:[10.1109/TMI.2008.920609](https://doi.org/10.1109/TMI.2008.920609)
- Alexander AL, Lee JE, Lazar M, Field AS (2007) Diffusion tensor imaging of the brain. *Neurotherapeutics* 4:316–329. doi:[10.1016/j.nurt.2007.05.011](https://doi.org/10.1016/j.nurt.2007.05.011)
- Arsigny V, Fillard P, Pennec X, Ayache N (2006) Log-euclidean metrics for fast and simple calculus on diffusion tensors. *Magn Reson Med* 56:411–421. doi:[10.1002/mrm.20965](https://doi.org/10.1002/mrm.20965)
- Assaf Y, Pasternak O (2008) Diffusion tensor imaging (DTI)-based white matter mapping in brain research: a review. *J Mol Neurosci* 34:51–61. doi:[10.1007/s12031-007-0029-0](https://doi.org/10.1007/s12031-007-0029-0)
- Azizi E, Brainerd EL, Roberts TJ (2008) Variable gearing in pennate muscles. *Proc Natl Acad Sci U S A* 105:1745–1750. doi:[10.1073/pnas.0709212105](https://doi.org/10.1073/pnas.0709212105)
- Basser PJ, Jones DK (2002) Diffusion-tensor MRI: theory, experimental design and data analysis—a technical review. *NMR Biomed* 15:456–467
- Basser PJ, Pajevic S (2000) Statistical artifacts in diffusion tensor MRI (DT-MRI) caused by background noise. *Magn Reson Med* 44:41–50. doi:[10.1002/1522-2594\(200007\)44:1<41::AID-MRM8>3.0.CO;2-O](https://doi.org/10.1002/1522-2594(200007)44:1<41::AID-MRM8>3.0.CO;2-O)

- Basser PJ, Pajevic S, Pierpaoli C, Duda J, Aldroubi A (2000) In vivo fiber tractography using DT-MRI data. *Magn Reson Med* 44:625–632
- Behrens TEJ, Woolrich MW, Jenkinson M et al (2003) Characterization and propagation of uncertainty in diffusion weighted MR imaging. *Magn Reson Med* 50:1077–1088. doi:10.1002/mrm.10609
- Bennett IJ, Rypma B (2013) Advances in functional neuroanatomy: a review of combined DTI and FMRI studies in healthy younger and older adults. *Neurosci Biobehav Rev* 37:1201–1210. doi:10.1016/j.neubiorev.2013.04.008
- Bley TA, Wieben O, Uhl M (2009) Diffusion-weighted MR imaging in musculoskeletal radiology: applications in trauma, tumors, and inflammation. *Magn Reson Imaging Clin N Am* 17:263–275. doi:10.1016/j.mric.2009.01.005
- Budzik JF, Le Thuc V, Demondion X, Morel M, Chechin D, Cotten A (2007) In vivo MR tractography of thigh muscles using diffusion imaging: initial results. *Eur Radiol* 17:3079–3085. doi:10.1007/s00330-007-0713-z
- Cermak NM, Noseworthy MD, Bourgeois JM, Tarnopolsky MA, Gibala MJ (2012) Diffusion tensor MRI to assess skeletal muscle disruption following eccentric exercise. *Muscle Nerve* 46:42–50. doi:10.1002/mus.23276
- Chi SW, Hodgson J, Chen JS, Reggie Edgerton V, Shin DD, Roiz RA, Sinha S (2010) Finite element modeling reveals complex strain mechanics in the aponeuroses of contracting skeletal muscle. *J Biomech* 43:1243–1250. doi:10.1016/j.jbiomech.2010.01.005
- Damon BM (2008) Effects of image noise in muscle diffusion tensor (DT)-MRI assessed using numerical simulations. *Magn Reson Med* 60:934–944. doi:10.1002/mrm.21707
- Damon BM, Ding Z, Anderson AW, Freyer AS, Gore JC (2002) Validation of diffusion tensor MRI-based muscle fiber tracking. *Magn Reson Med* 48:97–104. doi:10.1002/mrm.10198
- Deux JF, Malzy P, Paragios N et al (2008) Assessment of calf muscle contraction by diffusion tensor imaging. *Eur Radiol* 18:2303–2310. doi:10.1007/s00330-008-1012-z
- Drace JE, Pelc NJ (1994) Tracking the motion of skeletal muscle with velocity encoded MR imaging. *J Magn Reson Imaging* 4:773–778 PMID: 7865936
- Einstein A (1956) *Investigations on the theory of the Brownian movement*. Dover, New York
- Englund EK, Elder CP, Xu Q, Ding Z, Damon BM (2011) Combined diffusion and strain tensor MRI reveals a heterogeneous, planar pattern of strain development during isometric muscle contraction. *Am J Physiol Regul Integr Comp Physiol* 300:R1079–R1090. doi:10.1152/ajpregu.00474.2010
- Esposito A, Campana L, Palmisano A, De Cobelli F, Canu T, Santarella F, Colantoni C, Monno A, Vezzoli M, Pezzetti G, Manfredi AA, Rovere-Querini P, Maschio AD (2013) Magnetic resonance imaging at 7 T reveals common events in age-related sarcopenia and in the homeostatic response to muscle sterile injury. *PLoS ONE* 8:e59308. doi:10.1371/journal.pone.0059308
- Finni T, Hodgson JA, Lai AM, Edgerton VR, Sinha S (2003) Nonuniform strain of human soleus aponeurosis-tendon complex during submaximal voluntary contractions in vivo. *J Appl Physiol* 95:829–837. PMID: 12716873
- Froeling M (2012) DTI of human skeletal muscle: from simulation to clinical implementation. PhD thesis, Department of Biomedical Engineering, Technische Universiteit Eindhoven
- Froeling M, Nederveen AJ, Heijtel DF, Lataster A, Bos C, Nicolay K, Maas M, Drost MR, Strijkers GJ (2012) Diffusion-tensor MRI reveals the complex muscle architecture of the human forearm. *J Magn Reson Imaging* 36:237–248. doi:10.1002/jmri.23608
- Galbán CJ, Maderwald S, Uffmann K, de Greiff A, Ladd ME (2004) Diffusion sensitivity to muscle architecture: a magnetic resonance diffusion tensor imaging study of the human calf. *Eur J Appl Physiol* 93:253–262. doi:10.1007/s00421-004-1186-2
- Galbán CJ, Maderwald S, Uffmann K, Ladd ME (2005) A diffusion tensor imaging analysis of gender differences in water diffusivity within human skeletal muscle. *NMR Biomed* 18:489–498. doi:10.1002/nbm.975
- Gharibans AA, Johnson CL, Chen DD, Georgiadis JG (2011) Reconstruction of 3D fabric structure and fiber nets in skeletal muscle via in vivo DTI. *International society for magnetic resonance in medicine*, Montreal, May 2011, p 1154
- Gilbert RJ, Napadow VJ (2005) Three-dimensional muscular architecture of the human tongue determined in vivo with diffusion tensor magnetic resonance imaging. *Dysphagia* 20:1–7. doi:10.1007/s00455-003-0505-9
- Hagmann P, Jonasson L, Maeder P, Thiran JP, Wedeen VJ, Meuli R (2006) Understanding diffusion MR imaging techniques: from scalar diffusion-weighted imaging to diffusion tensor imaging and beyond. *Radiographics* 26(Suppl 1):S205–S223. doi:10.1148/rg.26si065510
- Hatakenaka M, Yabuuchi H, Matsuo Y et al (2008) Effect of passive muscle length change on apparent diffusion coefficient: detection with clinical MR imaging. *Magn Reson Med Sci* 7:59–63. pii:JST.JSTAGE/mrms/7.59
- Heemskerk A, Drost M, van Bochove G et al (2006) DTI-based assessment of ischemia-reperfusion in mouse skeletal muscle. *Magn Reson Med* 56:272–281. doi:10.1002/mrm.20953
- Heemskerk A, Strijkers G, Drost M, van Bochove G, van Nicolay K (2007) Skeletal muscle degeneration and regeneration after femoral artery ligation in mice: monitoring with diffusion MR imaging. *Radiology* 243:413–421. doi:10.1148/radiol.2432060491
- Heemskerk AM, Sinha TK, Wilson KJ, Ding Z, Damon BM (2009) Quantitative assessment of DTI-based muscle fiber tracking and optimal tracking parameters. *Magn Reson Med* 61:467–472. doi:10.1002/mrm.21819
- Heemskerk AM, Sinha TK, Wilson KJ, Ding Z, Damon BM (2010) Repeatability of DTI-based skeletal muscle fiber tracking. *NMR Biomed* 23:294–303. doi:10.1002/nbm.1463
- Hodgson JA, Finni T, Lai AM, Edgerton VR, Sinha S (2006) Influence of structure on the tissue dynamics of the human soleus muscle observed in MRI studies during isometric contractions. *J Morphol* 267:584–601. doi:10.1002/jmor.10421
- Karampinos DC, King KF, Sutton BP, Georgiadis JG (2007) In vivo study of cross-sectional skeletal muscle fiber asymmetry with diffusion-weighted MRI. *Conf Proc IEEE Eng Med Biol Soc* 2007:327–330. doi:10.1109/IEMBS.2007.4352290
- Karampinos DC, King KF, Sutton BP, Georgiadis JG (2009) Myofiber ellipticity as an explanation for transverse asymmetry of skeletal muscle diffusion MRI in vivo signal. *Ann Biomed Eng* 37:2532–2546. doi:10.1007/s10439-009-9783-1
- Karampinos DC, Banerjee S, King KF, Link TM, Majumdar S (2012) Considerations in high-resolution skeletal muscle diffusion tensor imaging using single-shot echo planar imaging with stimulated-echo preparation and sensitivity encoding. *NMR Biomed* 25:766–778. doi:10.1002/nbm.1791
- Lansdown DA, Ding Z, Wadlington M, Hornberger JL, Damon BM (2007) Quantitative diffusion tensor MRI-based fiber tracking of human skeletal muscle. *J Appl Physiol* 103:673–681. doi:10.1152/jappphysiol.00290.2007
- Lazar M (2010) Mapping brain anatomical connectivity using white matter tractography. *NMR Biomed* 23:821–835. doi:10.1002/nbm.1579
- Leemans A, Jones DK (2009) The B-matrix must be rotated when correcting for subject motion in DTI data. *Magn Reson Med* 61:1336–1349. doi:10.1002/mrm.21890
- Levin DI, Gilles B, Mädler B, Pai DK (2011) Extracting skeletal muscle fiber fields from noisy diffusion tensor data. *Med Image Anal* 15:340–353. doi:10.1016/j.media.2011.01.005

- Maganaris CN, Baltzopoulos V, Sargeant AJ (1998) In vivo measurements of the triceps surae complex architecture in man: implications for muscle function. *J Physiol* 512:603–614. PMID: 9763648
- Malcolm JG, Shenton ME, Rathi Y (2010) Filtered multi-tensor tractography. *IEEE Trans Med Imaging* 29:1664–1675. doi:10.1109/TMI.2010.2048121
- Martin DC, Medri MK, Chow RS, Oxorn V, Leekam RN, Agur AM, McKee NH (2001) Comparing human skeletal muscle architectural parameters of cadavers with in vivo ultrasonographic measurements. *J Anat* 199:429–434. PMID: 11693303
- McMillan AB, Shi D, Pratt SJ, Lovering RM (2011) Diffusion tensor MRI to assess damage in healthy and dystrophic skeletal muscle after lengthening contractions. *J Biomed Biotechnol* 2011:970726. doi:10.1155/2011/970726
- Mori S, Barker PB (1999) Diffusion magnetic resonance imaging: its principle and applications. *Anat Rec* 257:102–109. doi:10.1002/(SICI)1097-0185(19990615)257:3<102::AID-AR7>3.0.CO;2-6
- Mori S, van Zijl PC (2002) Fiber tracking: principles and strategies—a technical review. *NMR Biomed* 15:468–480. doi:10.1002/nbm.781
- Mori S, Crain BJ, Chacko VP et al (1999) Three-dimensional tracking of axonal projections in the brain by magnetic resonance imaging. *Ann Neurol* 45:265–269 PMID: 9989633
- Mukherjee P, McKinstry RC (2006) Diffusion tensor imaging and tractography of human brain development. *Neuroimaging Clin N Am* 16:19–43. doi:10.1016/j.nic.2005.11.004
- Muramatsu T, Muraoka T, Kawakami Y, Shibayama A, Fukunaga T (2002) In vivo determination of fascicle curvature in contracting human skeletal muscles. *J Appl Physiol* 92:129–134. PMID: 11744651
- Nakai R, Azuma T, Sudo M, Urayama S, Takizawa O, Tsutsumi S (2008) MRI analysis of structural changes in skeletal muscles and surrounding tissues following long-term walking exercise with training equipment. *J Appl Physiol* 105:958–963. doi:10.1152/jappphysiol.01204.2007
- Napadow VJ, Chen Q, Mai V, So PT, Gilbert RJ (2001) Quantitative analysis of three-dimensional resolved fiber architecture in heterogeneous skeletal muscle tissue using NMR and optical imaging methods. *Biophys J* 80:2968–2975. doi:10.1016/S0006-3495(01)76262-5
- O'Donnell LJ, Westin CF (2011) An introduction to diffusion tensor image analysis. *Neurosurg Clin N Am* 22:185–196. doi:10.1016/j.nec.2010.12.004
- Okamoto Y, Kunimatsu A, Kono T, Nasu K, Sonobe J, Minami M (2010) Changes in MR diffusion properties during active muscle contraction in the calf. *Magn Reson Med Sci* 9:1–8. pii:JST.J-STAGE/mrms/9.1
- Qi J, Olsen NJ, Price RR, Winston JA, Park JH (2008) Diffusion weighted imaging of the inflammatory myopathies: polymyositis and dermatomyositis. *J Magn Reson Imaging* 27:212–217. doi:10.1002/jmri.21209
- Pappas GP, Asakawa DS, Delp SL, Zajac FE, Drace JE (2002) Nonuniform shortening in the biceps brachii during elbow flexion. *J Appl Physiol* 92:238123–238129. doi:10.1152/jappphysiol.00843.2001
- Saupe N, White LM, Stainsby J, Tomlinson G, Sussman MS (2009) Diffusion tensor imaging and fiber tractography of skeletal muscle: optimization of B value for imaging at 1.5 T. *Am J Roentgenol* 192:W282–W290. doi:10.2214/AJR.08.1340
- Schwenzer NF, Steidle G, Martirosian P, Schraml C, Springer F, Claussen CD, Schick F (2009) Diffusion tensor imaging of the human calf muscle: distinct changes in fractional anisotropy and mean diffusion due to passive muscle shortening and stretching. *NMR Biomed* 22:1047–1053. doi:10.1002/nbm.1409
- Scollan DF, Holmes A, Winslow R, Forder J (1998) Histological validation of myocardial microstructure obtained from diffusion tensor imaging. *Am J Physiol* 275:H2308–H2318 PMID: 9843833
- Shenton ME, Hamoda HM, Schneiderman JS, Bouix S, Pasternak O, Rathi Y, Vu MA, Purohit MP, Helmer K, Koerte I, Lin AP, Westin CF, Kikinis R, Kubicki M, Stern RA, Zafonte R (2012) A review of magnetic resonance imaging and diffusion tensor imaging findings in mild traumatic brain injury. *Brain Imaging Behav* 6:137–192. doi:10.1007/s11682-012-9156-5
- Shin D, Finni T, Ahn S, Hodgson JA, Lee HD, Edgerton VR, Sinha S (2008) Effect of chronic unloading and rehabilitation on human achilles tendon properties: a velocity-encoded phase-contrast MRI study. *J Appl Physiol* 105:1179–1186. doi:10.1152/jappphysiol.90699.2008
- Sigmund EE, Sui D, Ukpebor O, Baete S, Fieremans E, Babb JS, Mechlin M, Liu K, Kwon J, McGorty K, Hodnett PA, Bencardino J (2013) Stimulated echo diffusion tensor imaging and SPAIR T(2)-weighted imaging in chronic exertional compartment syndrome of the lower leg muscles. *J Magn Reson Imaging*. doi:10.1002/jmri.24060
- Sinha S, Sinha U (2011) Reproducibility analysis of diffusion tensor indices and fiber architecture of human calf muscles in vivo at 1.5 tesla in neutral and plantarflexed ankle positions at rest. *J Magn Reson Imaging* 34:107–119. doi:10.1002/jmri.22596
- Sinha S, Sinha U, Edgerton VR (2006) In vivo diffusion tensor imaging of the human calf muscle. *J Magn Reson Imaging* 24:182–190. doi:10.1002/jmri.20593
- Sinha U, Sinha S, Hodgson JA, Edgerton RV (2011) Human soleus muscle architecture at different ankle joint angles from magnetic resonance diffusion tensor imaging. *J Appl Physiol* 110:807–819. doi:10.1152/jappphysiol.00923.2010
- Sinha U, Moghadassi A, Sinha S (2012) Strain rate mapping of the lower leg muscles during plantarflexion excursion using MR velocity mapping. *Int Soc Magn Res Med, Melbourne, Australia*. May 2012
- Tseng WY, Wedeen VJ, Reese TG, Smith RN, Halpern EF (2003) Diffusion tensor MRI of myocardial fibers and sheets: correspondence with visible cut-face texture. *J Magn Reson Imaging* 17:31–42. doi:10.1002/jmri.10223
- van Aart E, Sepasian N, Jalba A, Vilanova A (2011) CUDA-accelerated geodesic ray-tracing for fiber tracking. *Int J Biomed Imaging* 2011:698908. doi:10.1155/2011/698908
- Williams SE, Heemskerk AM, Welch EB, Li K, Damon BM, Park JH (2013) Quantitative effects of inclusion of fat on muscle diffusion tensor MRI measurements. *J Magn Reson Imaging*. doi:10.1002/jmri.24045
- Yamabe E, Nakamura T, Oshio K, Kikuchi Y, Toyama Y, Ikegami H (2007) Line scan diffusion spectrum of the denervated rat skeletal muscle. *J Magn Reson Imaging* 26:1585–1589. doi:10.1002/jmri.21184
- Zaraskaya T, Kumbhare D, Noseworthy MD (2006) Diffusion tensor imaging in evaluation of human skeletal muscle injury. *J Magn Reson Imaging* 24:402–408. doi:10.1002/jmri.20651